Wang et al. Biochar (2026) 8:46
https://doi.org/10.1007/s42773-025-00551-2

Biochar

ORIGINAL RESEARCH Open Access

Sustainable removals of antibiotics via biochar-enhanced ultrasound cavitation effect: synergy of carbon nanotube bonded biochar@Fe_3C composite and low frequency energy efficiency

Ao Wang[1†], Nan Zhao[2†], Lei He[1], Ye Xiao[1], Chuanfang Zhao[4], Siyuan Guo[1], Xiang Liu[5], Weihua Zhang[1*], Kunyuan Liu[1,3*] and Rongliang Qiu[1,6]

Abstract

The recalcitrant antibiotics of enrofloxacin (ENT) and amoxicillin (AMT) were difficult to remove by conventional sonication. To address this challenge, a new type of carbon nanotube covalently bonded biochar@Fe_3C composite (BCM@Fe) was first designed by calcination and employed as a solid cavitation material (SCM) under low-frequency ultrasound (US) conditions to accelerate the removals of ENT and AMT. Compared to conventional carbon nanotube@Fe_3C composites, BCM@Fe demonstrated significantly improved removal performance, achieving 15.5-fold and 3.50-fold higher removal rates for ENT and AMT, respectively. The removal efficiencies increased by 32.1–32.3% compared with a conventional shake system. Mechanistic studies revealed a dual removal mechanism involving simultaneous adsorption and degradation. The coupling of low-frequency ultrasound with BCM@Fe had synergistic effects; the US promoted the dispersion of the composites and inhibited H_2O-induced oxidation by generating surface-localized cavitation bubbles. Notably, BC in BCM@Fe was found to amplify cavitation effect with performance strongly correlated with material characteristics such as pH, carbonization degree, aromaticity, hydrophobicity, and graphitization. Degradation differed between antibiotics: the degradation of ENT predominantly occurred at the material surface, while that of AMT took place in the liquid phase. Overall, the successful access to low-cost SCM integrating with low-frequency ultrasound made the possible for potential application in antibiotic wastewater.

Highlights

- Biochar increased hydrophobicity, aromatization, graphitization and pH of BCM@Fe.
- Biochar enhanced cavitation effect for removals of enrofloxacin and amoxicillin.
- US enhances the dispersion of solid cavitation material and prevents oxidation.
- Ethanol washing quantifies the contribution of cavitation effect.

[†]Ao Wang and Nan Zhao have contributed equally to this work.

*Correspondence:
Weihua Zhang
zhangwh5@mail.sysu.edu.cn
Kunyuan Liu
liuky@ms.giec.ac.cn
Full list of author information is available at the end of the article

Springer

- ENT degrades on the surface of SCM, while AMT degrades in the liquid phase.

Keywords Biochar, Solid cavitation material, Antibiotics degradation, Low-frequency ultrasound, Cavitation effect

Graphical Abstract

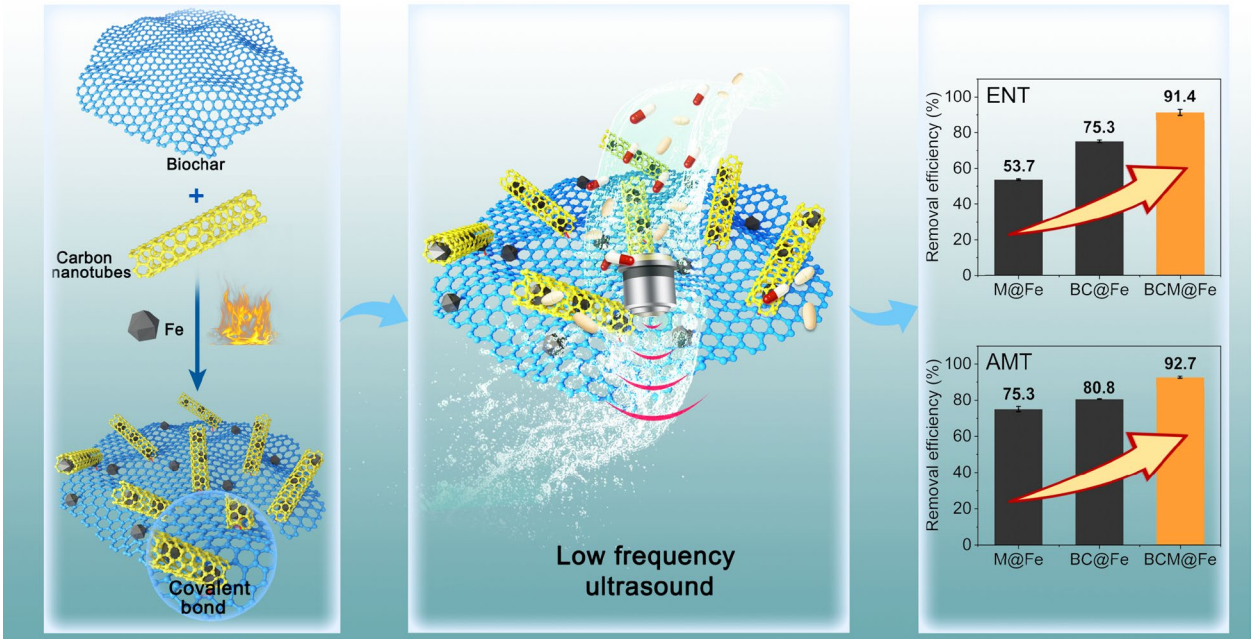

1 Introduction

Antibiotics are essential in the treatment of bacterial infections in both humans and animals. However, their extensive use and low utilization efficiency have led to their accumulation in the environment (Lu et al. 2025; Singh and Kim 2025; Yi et al. 2025). Enrofloxacin (ENT) and amoxicillin (AMT) are broad-spectrum antibiotics that have been widely applied and identified in wastewater (Li et al. 2020; Wada and Olawade 2025). The pharmaceutical wastewater contains elevated concentrations of antibiotics, with the concentration of ENT reaching up to 1.0 mmol L^{-1}, and that of AMT has been documented at 100–140 mg L^{-1} (Luan et al. 2022; Wang et al. 2024a, b). Nevertheless, their hydrophobic properties and low numbers of hydrogen-bond acceptors or donors, as indicated in Table S1, render them particularly resistant to degradation compared with other antibiotics (Bergamonti et al. 2019; Kowalska et al. 2021; Peng et al. 2019). Additionally, internal exposure of ENT brings the obesity risk in children, and AMT exposure can cause hepatotoxicity (Fontana et al. 2005; Shan et al. 2022). Consequently, it is imperative to develop effective strategies for the elimination of these antibiotic pollutants from the environment.

Conventional sonication is a green technology for degrading organic pollutants because ultrasonic waves in water induce chemical reactions through the formation and collapse of cavitation bubbles, resulting in the generation of localized hot spots and ROS of free radicals or singlet oxygen ($^1O_2$) to destroy antibiotics (Flint and Suslick 1991; Gutiérrez et al. 1986). However, a consecutive input of high-frequency ultrasound is necessary to produce more competent internal cavitation bubbles for sufficient production of reactive oxygen species (ROS), due to the slow and spatiotemporally random bubble nucleation (Liu et al. 2023a, b; Thomas et al. 2019). Meanwhile, high-frequency ultrasound is energy-intensive but exhibits low removal efficiency for antibiotics; for example, ultrasound at 120–130 kHz degrades only 5–30% of antibiotics but requires 500–750 W of power (Gholami et al. 2016; Rahmani et al. 2014). Sonication-catalysis has been demonstrated as a promising alternative to accelerate the degradation of antibiotics (Cui et al. 2023). Solid catalysts such as Fe^0

and Fe_3O_4 can induce Fenton-like process to enhance antibiotic degradation under ultrasound by generating additional oxidizing radicals (Cui et al. 2023; Dehghan et al. 2018). However, the dispersion of Fe particles in water may be challenging because of their high density and hydrophilic surface (Peng et al. 2018). Furthermore, significant release of Fe ions leads to the production of Fe sludge, which might cause secondary pollution (Zhao et al. 2020).

Dealing with these problems, nano-confined Fe particles covered by hydrophobic carbon nanotubes (CNTs) have been developed to mediate the Fenton reaction with H_2O_2 (Yang et al. 2019). Yet, using only CNTs as an Fe support seemed not particularly desirable, with 27% antibiotics removal efficiency in 40 min treatment (Zhang et al. 2022). To suppress the agglomeration and accelerate the dispersion, functionalized CNTs such as hydrophilic hybrid material of oxidized CNTs@quaternized hyperbranched polyethyleneimine was synthesized (Sapalidis et al. 2018). However, it should be noted that the synthesized material may cause the loss of hydrophobicity (Wu et al. 2022), and greater hydrophilicity of the surface disfavors cavitation formation (Thomas et al. 2019). Biochar (BC), a kind of macromolecular carbon material with hydrophobicity, was obtained by pyrolyzing the biomass precursor. It has been used to combine with CNTs for enhancing antibiotic adsorption (Inyang et al. 2015), but the specific interaction mechanisms between CNTs and BC remain unexplored. A previous study has suggested that graphitic carbon nitride-based material could be formed by melamine self-assembly with macromolecular graphene through covalent C-N bonds to maintain structural integrity (Zhang et al. 2019). Thus, it is hypothesized that a composite with higher hydrophobicity, serving as a support for Fe particles to promote cavitation and maintaining structural stability, could be synthesized by covalently combining BC and melamine under pyrolysis conditions.

To validate this hypothesis, a novel CNT-covalently bonded BC@Fe_3C (BCM@Fe) composite was first fabricated and applied as a solid cavitation material (SCM) to remove ENT and AMT under sonocatalysis conditions. Thereafter, the morphology, structures and chemical compositions of the BC@Fe_3C composites were comprehensively investigated. The as-synthesized BCM@Fe composite had the highest hydrophobicity and graphitization degree compared with the carbon nanotube@Fe_3C (M@Fe) and biochar@Fe^0 (BC@Fe) composites. Moreover, BCM@Fe showed excellent adsorption and degradation capacities in treating antibiotic wastewater, especially in a wide pH window. The adsorption and degradation mechanisms for antibiotic elimination over the composites were studied by X-ray photoelectron spectroscopy (XPS), quenching tests, and electron paramagnetic resonance (EPR). Finally, the degradation products were analyzed by ultra-performance liquid chromatography-quadrupole time-of-flight-mass spectrometry (UPLC-QTOF-MS/MS), and the degradation pathways were proposed.

2 Materials and methods

2.1 Ultrasonic degradation tests

Batch kinetic tests were initiated by mixing 10 mg of a composite with 15 mL of 0.08 mM ENT or AMT with natural pH in 50 mL brown glass bottles. Then, the mixture was sonicated in a KQ-5200/KQ-2200 ultrasound washer (Kunshan Ultrasound Instruments Co., Ltd, Jiangsu, China) for 10, 20, 30, 40, 60, 120, 180, 240, and 360 min at 200 W/40 kHz and 100W/20 kHz low frequencies. The temperature was kept at ~ 30 °C by adding ice packs. Subsequently, the mixture was centrifuged and the supernatant was filtered through a 0.22 μm polytetrafluoroethylene filter. Batch adsorption tests were also conducted using a shaker (Zhichu Instruments, ZQZY-AGF8E) as the control. The other procedures were the same as the ultrasonic tests. The concentrations of ENT and AMT were monitored by a high-performance liquid chromatography (HPLC, Dionex Ultimate 3000) system with a variable wavelength detector at 278 and 254 nm, respectively. Chromatographic separation was performed on an Agilent InfinityLab Poroshell 120 EC-C18 column (4.6×50 mm, 2.7 μm). The mobile phase consisted of 82.5% phosphate and 17.5% acetonitrile for ENT analysis, while that was 92.0% phosphate and 8.0% acetonitrile for AMT, at an isocratic flow rate of 1 $mLmin^{-1}$. The retention time was 3.8 and 1.6 min for ENT and AMT, respectively. Total organic carbon (TOC) was determined by a TOC analyzer (Vario TOC, Germany), and the solution pH was measured by a multi-parameter analyzer (FE22-standard, Mettler Toledo). The energy density (ED) is defined as the ultrasonic energy delivered per unit volume of the treated suspension, calculated according to the following equation (Serna-Galvis et al. 2025):

$$ED = \frac{P \times t}{V}$$

where P is the ultrasonic power (W), t is the sonication time (h), and V is the sample volume (mL).

2.2 Desorption experiment

To detect the degradation intermediate products of ENT adsorbed on the materials, the reacted BCM@Fe composite was mixed with eluents consisting of methanol and various proportions of ammonia (0%, 5%, 10%, 15%, and 20%) at a ratio of 1 mg to 1.5 mL and shaken at 180 rpm min^{-1}. As illustrated in Fig. S1, methanol

containing 15% aqueous ammonia exhibited the highest ability to desorb ENT and more ENT was obtained when the desorption time was 12 h. Hence, 12 h and 15% ammonia in methanol were selected for further experiments. Methanol, ethanol, ethanol/ammonia mixture solution, 0.1 M HCl, and 0.15 M NaOH were used as the desorption agents for desorbing AMT that was adsorbed by BCM@Fe, respectively. However, no AMT in the eluent was detected because little AMT was adsorbed on the material.

3 Results and discussion

3.1 Structural characterization of BCM@Fe

The SEM image in Fig. 1a displayed that BCM@Fe had the dual structures of BC and CNTs. CNTs were rooted to BC matrixes and grew along a direction perpendicular to the surface of BC, with a diameter of ~ 100 nm. The white particles wrapped on the top of CNTs were Fe particles, and they acted as a catalyst to promote the growth of CNTs during the material synthesis process (Zhao et al. 2023). The Fe particles of BC@Fe were irregularly

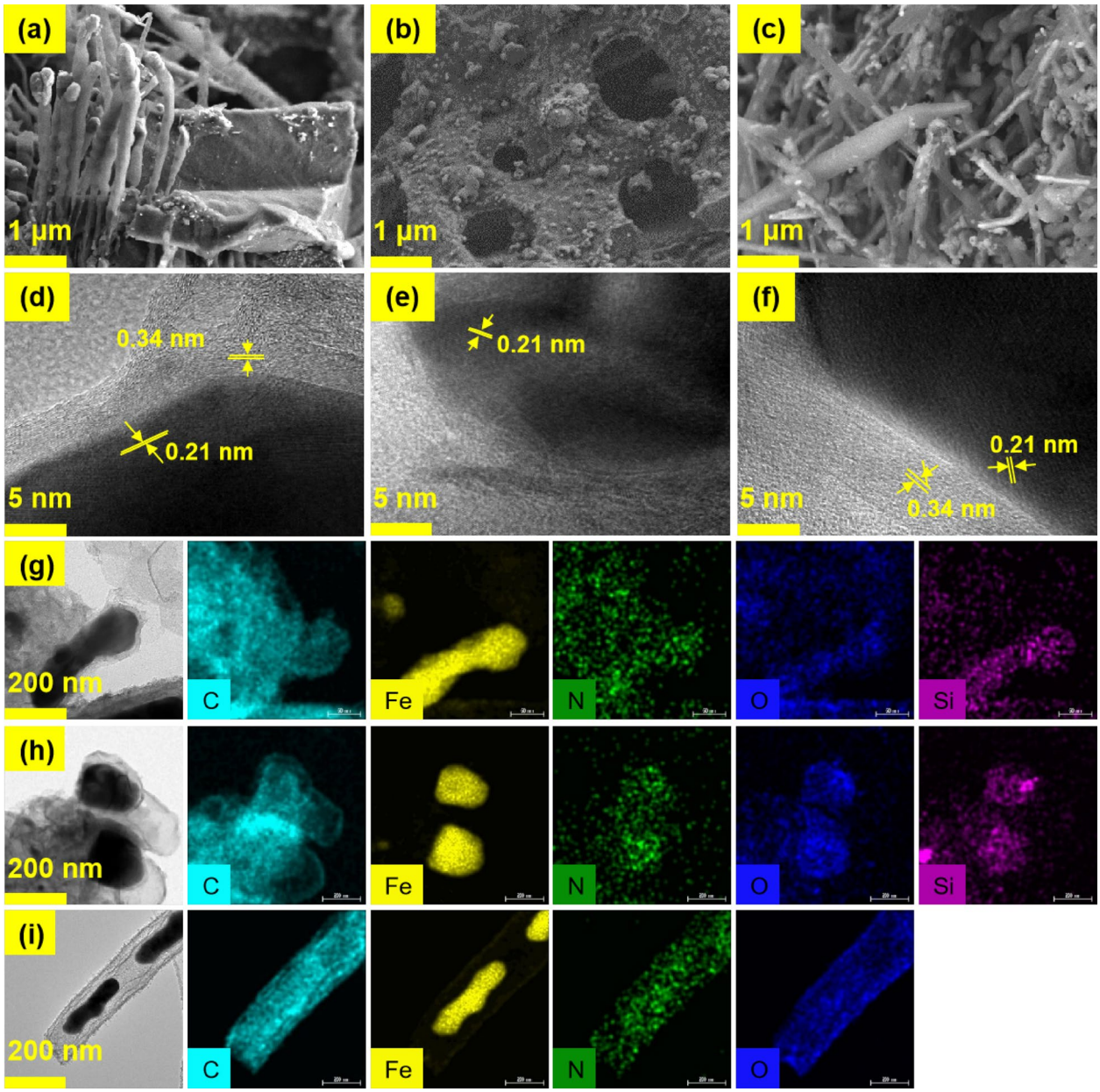

Fig. 1 SEM, high resolution TME images, and TEM-elemental mappings of BCM@Fe (**a**, **d**, **g**), BC@Fe (**b**, **e**, **h**), and M@Fe (**c**, **f**, **i**)

distributed on the surface of BC or embedded in the BC matrix (Fig. 1b). The CNTs of M@Fe were 70–200 nm in diameter and the Fe particles were filled in the tubes (Fig. 1c). Figure 1d shows a high-resolution image of an Fe particle. The lattice width of the gray part was 0.34 nm, corresponding to the graphite crystal (002). The edge lattice width of the black Fe sphere was 0.21 nm, indicating the formation of the Fe_3C (110) crystal plane. The TEM image of BCM@Fe (Fig. 1d) confirmed that its microstructure mainly contained two kinds of carbon structures. One was a thin sheet of graphene-phase biochar structure, and the other was a short CNT structure. For BC@Fe, the Fe spheres with diameters of 50–60 nm were wrapped in the graphite layer (Fig. 1e). Figure 1f shows the architecture of M@Fe, in which the Fe particles with the diameters of 80 nm were filled in multi-walled CNTs with outer and inner diameters of about 150 and 90 nm. TEM-mapping images of the composites (Figs. 1g–i) showed that N and O elements were homogeneously distributed on the carbon layers. In BCM@Fe and BC@Fe, the distribution of Si element predominantly centered around regions containing Fe particles, signifying a strong interaction between Fe and Si (Francisco et al. 2020). The tubular structure in BCM@Fe was uniformly distributed with Si element which was derived from BC, implying that BC provided feedstocks for supporting CNTs growth.

Figure 2a shows the XRD patterns of the composites. BCM@Fe and M@Fe had similar peaks at 37.75°, 42.89°, 45.87°, 51.83°, 70.84°, and 83.05°, which were assigned to Fe_3C. The peaks at 44.72°, 65.20° and 83.03° represented the diffraction peaks of Fe^0 for BC@Fe (Zhao et al. 2019). The diffraction peak of graphite carbon (002) was only formed in BCM@Fe, indicating that the combination of BC and melamine promoted the formation of a graphite carbon structure. The N_2 adsorption–desorption isotherms of the composites shown in Fig. 2b were all typical VI isotherm curve with a H1 hysteresis hoop, and the specific surface area for BCM@Fe, BC@Fe and M@Fe were 191, 457, and 100 m^2g^{-1}, respectively (Table S2). Compared to M@Fe, the introduction of BC guaranteed a bigger specific surface area and a larger micropore volume for BCM@Fe.

The C contents of BCM@Fe (49.8%) and BC@Fe (49.5%) were larger than that of M@Fe (37.8%, Table S3), suggesting that the introduction of BC increased the carbonization degree. Due to the dehydrogenation oxidation and condensation reactions between melamine and BC (Rangraz and Heravi 2021), the H content of BCM@Fe (0.35%) was significantly ($p < 0.001$) lower than those of BC@Fe (0.85%) and M@Fe (0.71%). The obviously reduced O content ($p < 0.01$), O/C value ($p < 0.01$), and (O + N)/C value ($p < 0.05$) for BCM@Fe suggested that the stability and hydrophobicity of the material were improved due to the decline of oxygen containing groups (Zhao et al. 2021, 2024a, b). Meanwhile, the reduction of acidic oxygen containing groups also caused a higher pH of BCM@Fe. The C/N value in BCM@Fe was smaller than that of BC@Fe, indicating that the existence of melamine increased the content of N functional groups. The H/C value of BCM@Fe was 0.08, which was much lower than 0.21 and 0.24 of BC@Fe and M@Fe, suggesting a higher degree of aromatization (Zhao et al. 2022). XPS results showed that the C, N and O contents on the surface of BCM@Fe were similar to those of M@Fe (Fig. 2d), but different from those of BC@Fe. These results agreed well with the bulk elemental analysis. The Fe content on the surface of M@Fe was the lowest (0.56%); however, that in the bulk was the highest (20.8%). This explained that most of the Fe particles were wrapped with graphite structures. Figure 2e shows the Fourier transform infrared (FT-IR) spectra of the composites, and the combination of CNTs with BC had profound effects on the surface functional groups. The bands at 1630–1637, 1452, and 882 cm^{-1} represented C = C, C–H bonds in alkane and aromatic phenyl, respectively. The peak at 882 cm^{-1} occurred only in BCM@Fe, showing that BCM@Fe was the most aromatic and had the maximum hydrophobic adsorption sites (Hontoria-Lucas et al. 1995). The peaks at 427–478 cm^{-1} represented the Fe–O functional group on BCM@Fe and BC@Fe (Liu et al. 2023a, b), and no peak appeared in M@Fe, indicating that more Fe particles in BCM@Fe and BC@Fe were exposed on the surface, and those in M@Fe were confined inside the CNT structures. This was consistent with the XPS results in Fig. 2.

Figure 2f shows the Raman spectra of BCM@Fe, BC@Fe and M@Fe, which all had D and G peaks (1350–1370 cm^{-1} and 1580–1600 cm^{-1}) within the test range. The I_D/I_G values of BCM@Fe, BC@Fe and M@Fe were 0.93, 0.97 and 0.99, respectively, indicating that the graphitization degree of BCM@Fe was the largest. A 2D peak (~ 2702 cm^{-1}) was associated with BCM@Fe and M@Fe composites, which was not shown in BC@Fe. This suggested the formation of CNTs structure in BCM@Fe and M@Fe (Çakmakçı et al. 2024). Nucleus-Independent Chemical Shifts (NICS) were used as an aromaticity probe and were further determined for the changes of aromaticity (Chen et al. 2005). The negative value of NICS represented the aromaticity of the aromatic ring, that was, the larger the absolute value of NICS, the greater the aromaticity of the selective aromatic ring. In this study, the aromaticity of multiple benzene rings was calculated by simulating BC, CNTs, and their composite materials in the same region, and the average value of NICS was used for comparison of aromaticity.

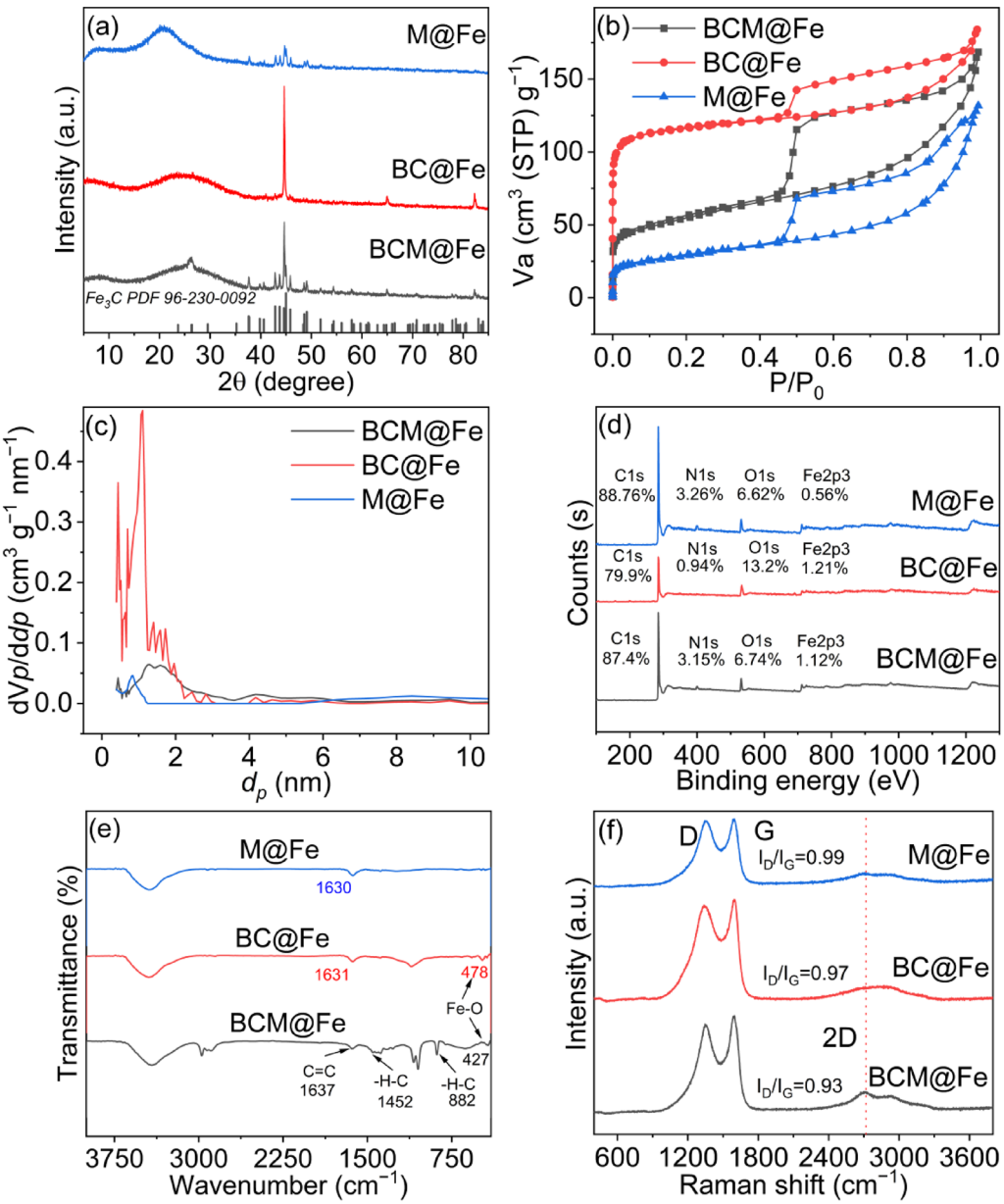

Fig. 2 XRD (**a**), BET (**b**), pore size distribution (**c**), XPS (**d**), FT-IR (**e**) and Raman (**f**) images of BCM@Fe, BC@Fe, and M@Fe

For saving computational time and cost, CNTs and BC in this study were represented by graphene layers and naphthol, respectively. The carbon carrier of BCM@Fe was a complex of naphthol and graphene. Two H atoms in naphthol were removed and the connected C atoms were combined with the C atoms in CNTs through the formation of two C–C covalent bonds (Fig. 3a, b). Based on this structure, the NICS values of the same region in the single graphene layer, naphthol, as well as their complex material, were calculated separately. As shown in Fig. 3c, there was no significant change in the aromaticity of the CNTs portion in the composite material, while the aromaticity of the BC portion was significantly enhanced. This revealed that the increased aromaticity of BCM@Fe was caused by the enhancement of aromaticity of BC. Thus, the introduction of BC increased the hydrophobicity, aromatization, graphitization and pH of BCM@Fe.

3.2 Removal behaviors of ENT and AMT by SCM

As shown in Fig. S2, reducing the US frequency and power from 40 kHz/200 W to 20 kHz/100 W led to a noticeable decline in removal efficiency, from 91.4

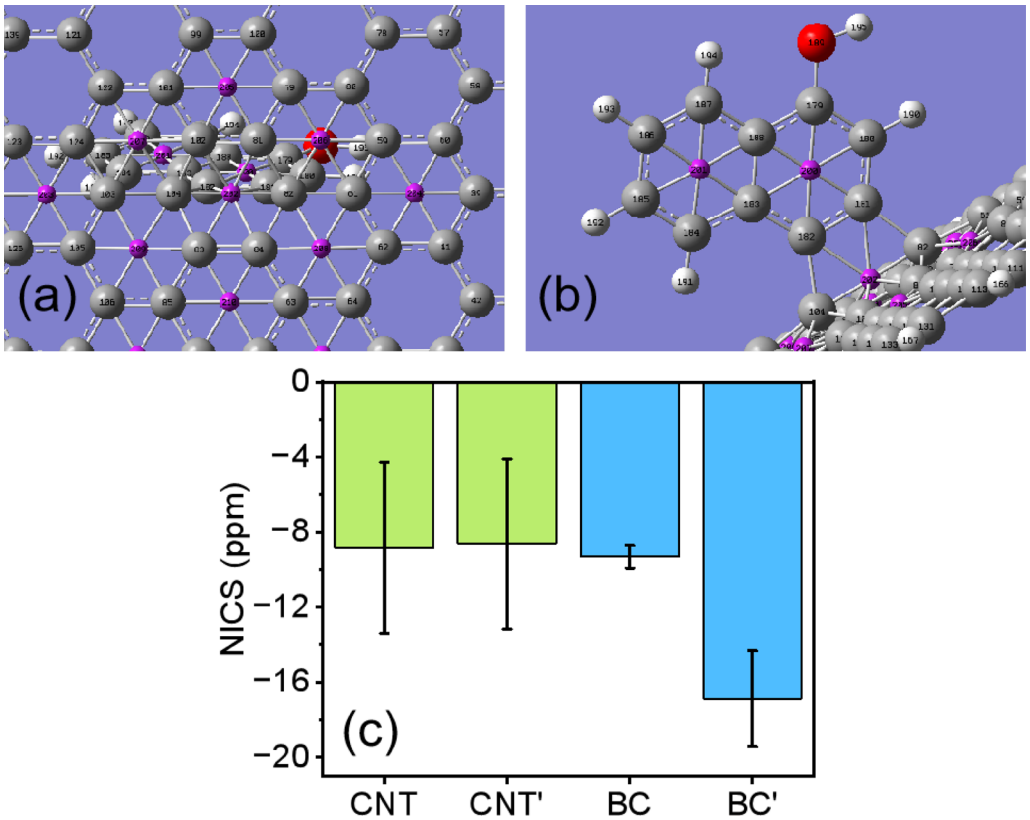

Fig. 3 The CNT and BC structures displayed in BCM@Fe (**a**, **b**); NICS values of CNT and BC before and after covalent combination (**c**)

to 72.0% for ENT, and from 92.9 to 66.3% for AMT by BCM@Fe. These results highlight the critical role of adequate US parameters in sustaining cavitation activity and achieving high degradation efficiency. Therefore, the US condition of 40 kHz/200 W was employed in all subsequent experiments.

Figure 4a and b displayed the removal kinetics of ENT and AMT by three materials in US and shake systems. The removal efficiency of the materials for both antibiotics was significantly enhanced by US compared to shaking. The removal efficiencies of ENT and AMT were 91.4% and 92.7% by BCM@Fe at 6 h, respectively. The removal kinetics were fitted with zero-order, pseudo first-order and pseudo second-order kinetic models (Table S4). BCM@Fe showed the best removal performances for ENT and AMT with pseudo-second-order kinetic rate constant (k_2) of 17.2 and 25.9 mM^{-1} h^{-1}, which were 2.24–2.52 and 3.50–15.5 times higher than those of BC@Fe and M@Fe, respectively (Fig. 4c, d). The coupling of BCM@Fe with low frequency ultrasound showed a better removal performance than the coupling of Fe–N–C@ZnO with photocatalysis, and N-TiO_2 with sonophotocatalysis (Tabel S5) (Geng et al. 2023; Karim and Shriwastav 2021). The TOC removal efficiencies for ENT and AMT by each material ranged from 48.7–76.9% and 33.1–57.1% in the US system at 6 h, respectively, which were significantly higher than those in the shake system (Fig. 4e, f). Meanwhile, BCM@Fe treatment also exhibited notably higher TOC removal efficiencies than the other two materials, which was in accordance with the results of removal kinetics experiments. The higher removal efficiencies and lower TOC removal efficiencies of AMT than those of ENT suggested that most of the degradation for AMT might occur in the solution. Further, ED was used to normalize the ultrasonic treatment conditions and to allow comparison between different materials. At the point where the removal efficiency of ENT reached 50%, the corresponding ED values for BCM@Fe, BC@Fe, and M@Fe were approximately 16.7, 33.4 and 300 W h L^{-1}, respectively. For AMT, the corresponding ED values for BCM@Fe, BC@Fe and M@Fe were approximately 33.4, 66.8 and 100 W h L^{-1}, respectively. This significantly lower energy requirement highlights the potential of BCM@Fe for more sustainable water treatment applications.

The effects of pH on the removal behaviors of antibiotics are shown in Fig. S3a-b. BCM@Fe achieved significantly removals of ENT and AMT in a wide pH rang

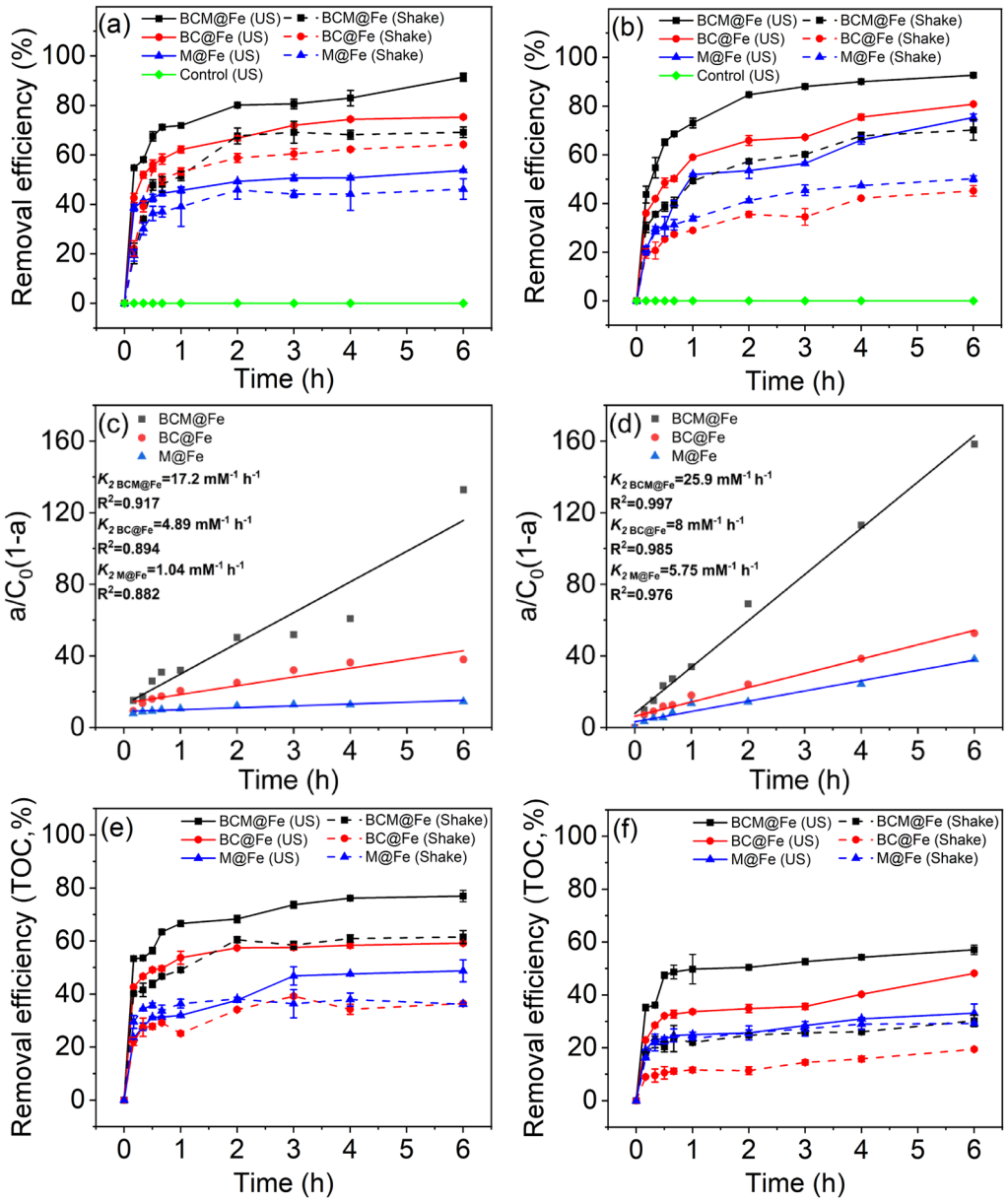

Fig. 4 The removal efficiencies, removal kinetics, and TOC removal efficiencies of ENT (**a**, **c**, **e**) and AMT (**b**, **d**, **f**) on the samples

of 4–10 in US condition and the removal efficiencies were > 77.9%. The highest removal efficiency of ENT on BCM@Fe was obtained at pH 7. This was because ENT had two pK_a values of 6.27 and 8.30 (Peng et al. 2019) and it was in its zwitterionic form ($ENT^{\pm}$) with low solubility and high hydrophobicity at pH 7 (Li et al. 2014). The hydrophobic interaction between ENT and BCM@Fe might play a major role in the adsorption process, which was the first step for removal. The pH at the point of zero charge (pH_{pzc}) for BCM@Fe, BC@Fe and M@Fe was 6.15, 6.15 and 5.40, respectively (Fig. S3c). During the reaction with ENT at pH 4 and 10, the surfaces of BCM@Fe composites were positively and negatively charged, respectively. The same charge between ENT and BCM@Fe composite resulted in electrostatic repulsion, which reduced the removal of ENT, thus, electrostatic attraction was not the reason for ENT adsorption. AMT possessed three proton-binding sites (carboxyl, amine and phenolic hydroxyl) with pK_a values of 2.40, 7.40 and 9.60 (Dou et al. 2020) and it also existed in its zwitterionic form at pH 4 and 7. But the removal efficiency of AMT on BCM@Fe at pH 7 was significantly lower than that at pH 4 (Fig. S3b), which suggested the potential occurrence of Fenton-like degradation.

3.3 SCM dispersion and stability as affected by US

The hydrodynamic diameter (D_h) refers to the apparent diameter of a particle in suspension as determined by dynamic light scattering, which reflects not only the core particle size but also the associated solvation layer and any surface-bound molecules (Maguire et al. 2018). Furthermore, the dispersion of materials in the medium significantly influenced mass transfer in the liquid (Grilla et al. 2020), which could be quantified by the D_h. As demonstrated in Fig. 5a–c, the D_hs values of BCM@Fe, BC@Fe, and M@Fe were decreased by 71%, 71%, and 61.1% after US for 0.5 h, respectively. Conversely, those were increased in the shake system, indicating that shaking restricted the dispersion because of the presence of hydrogen bonding and van der Waals forces among the materials (Tan et al. 2021). Additionally, the correlation analysis unveiled a significant negative correlation between D_hs values and the removal efficiencies of ENT and AMT by the materials after 0.5 h of reaction ($p < 0.01$, $r = -1.00$). Therefore, US promoted the dispersion of the materials through exposing more active sites to enhance the removal of ENT and AMT by the materials.

Figure 6 shows the XRD patterns of the materials after reaction with 0.08 mM ENT and AMT in the US system. During the reaction with antibiotics, Fe_3C in BCM@Fe kept its original state and the oxidation peaks of Fe_3O_4 (PDF 97-002-0596) appeared at 6 and 4 h for ENT and AMT, respectively. There were barely released Fe concentrations (0.1 mgL^{-1}) in the liquid by BCM@Fe during US treatment at equilibrium (Fig. S4a–b). By comparing the XRD patterns of three materials after reactions for 0.5 h in US and shake systems (Fig. S5a–f), it was found that the Fe crystal phase was significantly and rapidly corroded in the shake system. The hydrolysis of Fe^{2+} led to a more noticeable reduction in the pH of ENT solution in shake system (Eq. 1, Fig. S5a) as compared to that of US treatment. More importantly, US could prevent acidification and conserve the materials' pH (Farshbaf Aghajani et al. 2023). Thus, US stimulation not only reinforced the removal efficiencies of antibiotics but also prevented the oxidization of materials by H_2O because the contact of the materials with H_2O were effectively inhibited by the cavitation bubbles created on the materials' surfaces. The stability of BC@Fe was significantly lower than that of BCM@Fe and M@Fe because the existence of CNT structures could cover Fe particles to increase the stability (Fig. 7).

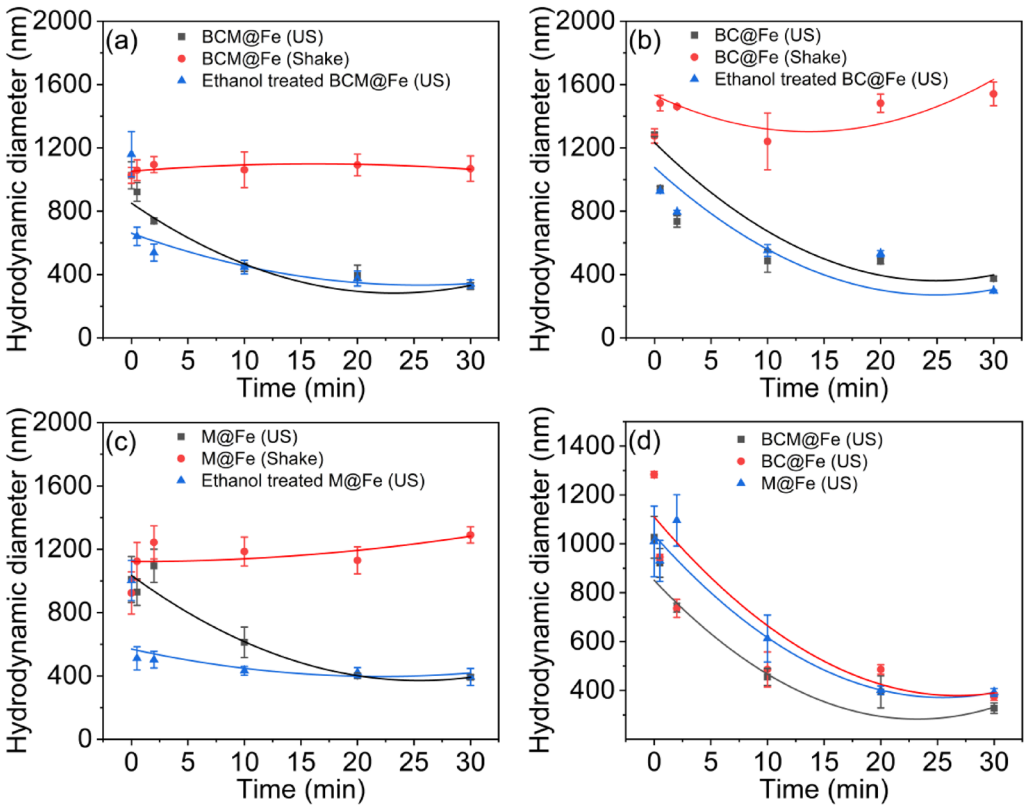

Fig. 5 Hydrodynamic diameter and contact angles of BCM@Fe (**a**), BC@Fe (**b**), and M@Fe (**c**) before and after ethanol treated under shake and US systems

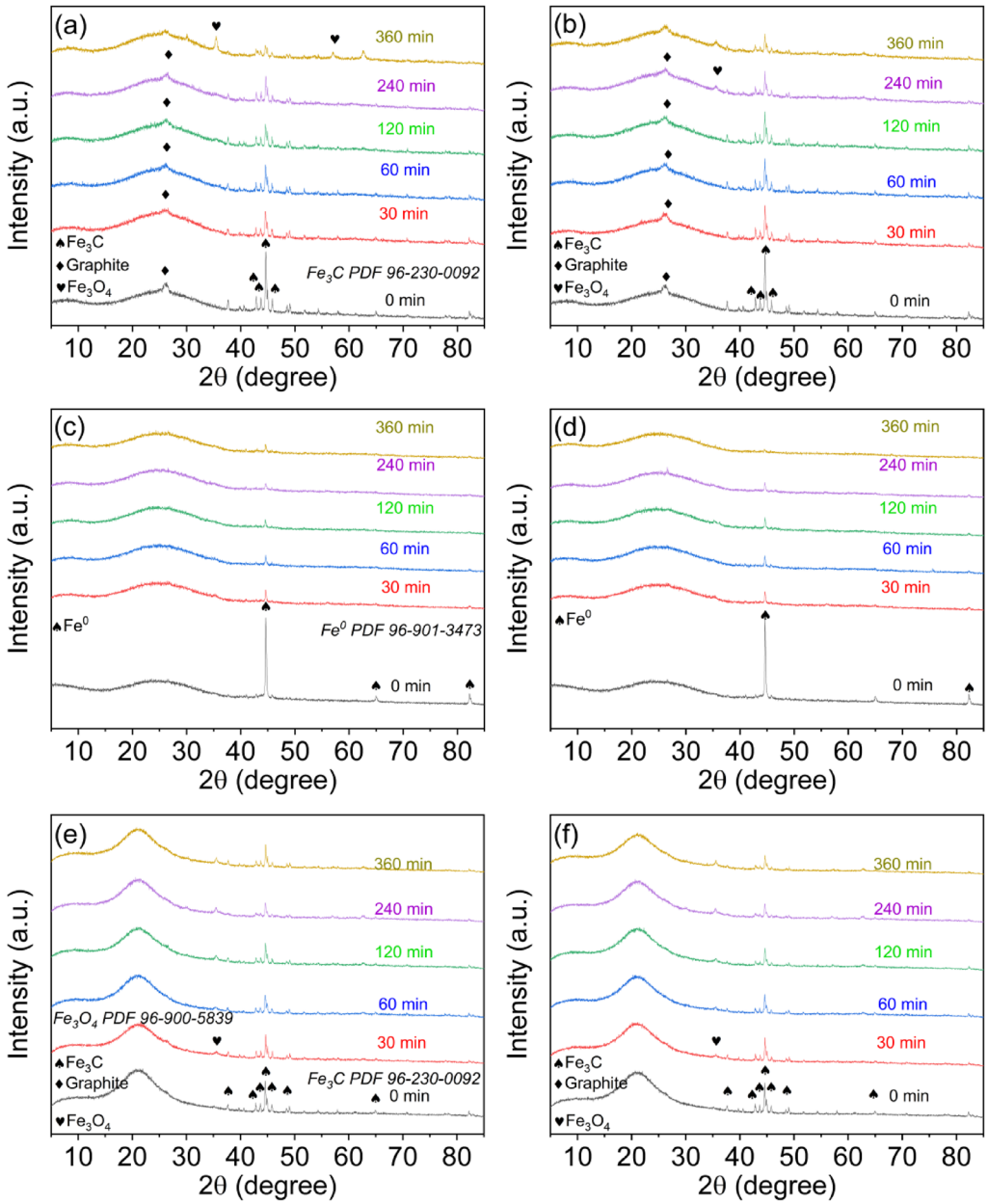

Fig. 6 XRD patterns of BCM@Fe, BC@Fe, and M@Fe before and after removals of ENT (**a**, **c**, **e**) and AMT (**b**, **d**, **f**)

$$3Fe^{2+} + 4H_2O \rightarrow Fe_3O_4 + H_2 + 6H^+ \quad (1)$$

3.4 Removal mechanisms of antibiotics by SCM under US system

3.4.1 Adsorption mechanisms

In order to explore the adsorption mechanisms of ENT/AMT, XPS spectra of the composites before and after the reaction was analyzed (Fig. 7). The percentage of C–C/C=C in the C1s spectra of BCM@Fe was 58.0%, and increased to 72.4% and 73.6% after the reactions with ENT and AMT, respectively. The enhancement explained the presence of π-π interaction (Li et al. 2024), which did not occur in BC@Fe and M@Fe composites. Thus, the increased aromaticity of CNT covalently bonded BC mediated the improved adsorption capacity. After the removal of ENT, the peak positions of C=O and C–O in BCM@Fe as well as C–O in M@Fe were shifted to lower binding energies. This was due to the formation of H bonds (Zhao et al. 2024a, b). AMT also formed H bonds with the oxygen containing groups of three materials.

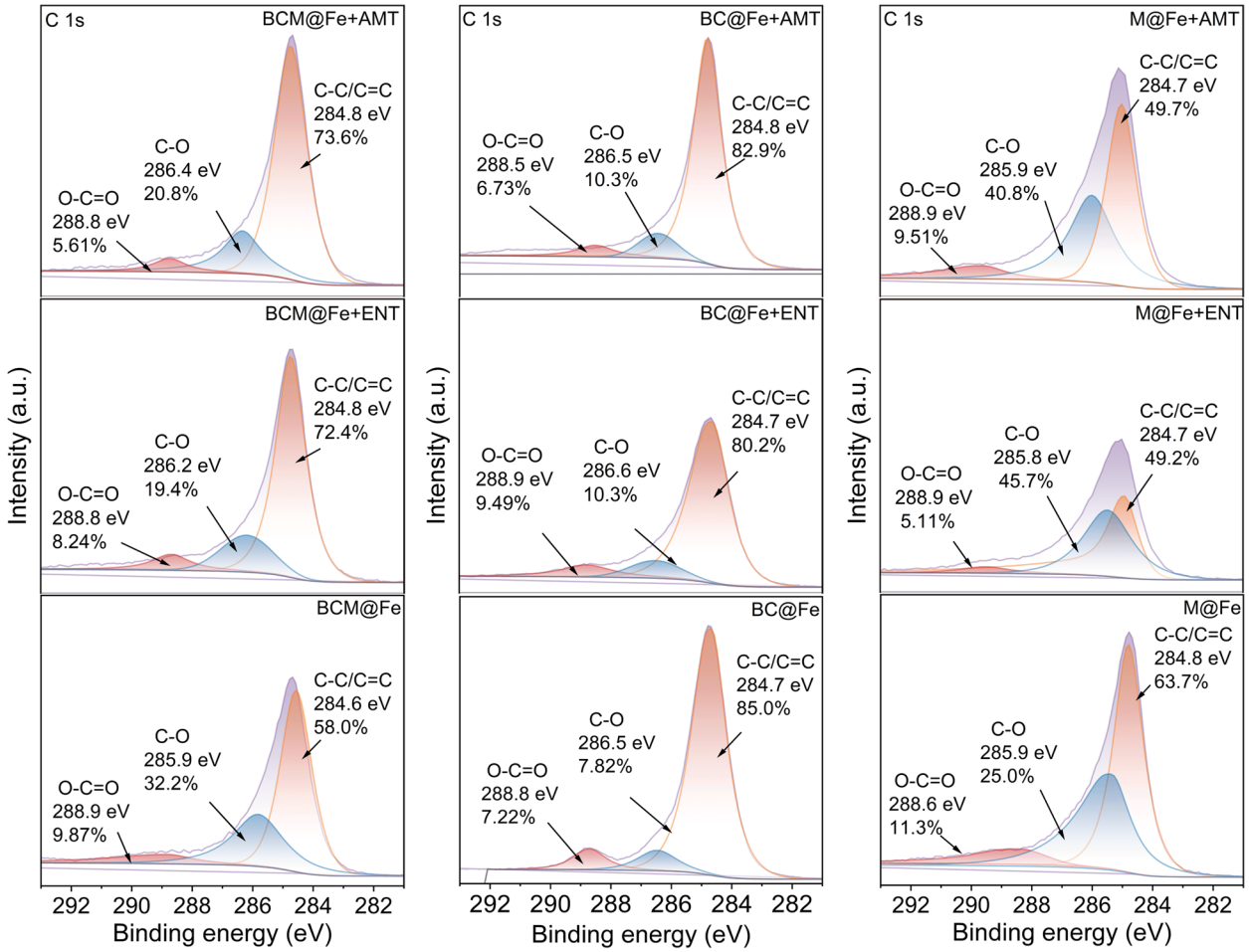

Fig. 7 The C1s XPS spectra of BCM@Fe, BC@Fe, and M@Fe before and after removals of ENT and AMT

Further, density functional theory (DFT) calculation indicated that the O atoms in the carboxylic group of ENT and AMT or the O atom in the hydroxyl group of AMT formed H bonds with the H atoms in the hydroxyl group of graphene ($\Delta G = -40.1$ and -60.2 kcalmol^{-1}, Fig. S6).

3.4.2 Degradation mechanisms

Ultrasound alone could not remove ENT and AMT in this study (Fig. 4a, b), due to the low probability of cavitation events at very low ultrasound frequency (Meroni et al. 2022). But the removal occurred effectively when SCM was present because they decreased the threshold for the occurrence of cavitation. The cavitation effect caused by US played a key role in the process of sonocatalysis, but few studies quantified its contribution to the degradation of pollutants.

When solid particles were introduced to the sonication medium, the hydrophobic interface and gas bubble stability provided by the materials were beneficial for the removal of organic pollutants (Stride and Coussios 2019). Ethanol washing treatment could reduce the hydrophobicity of materials as indicated by the decreased contact angle (Fig. S7) and it also "neutralized" the bubble stability through removing the gas bubble from the surface, so that it could effectively limit the probability of cavitation between the SCM and liquid in the US system (Jonnalagadda et al. 2022). As shown in Fig. 8a, b, the ethanol-washed materials had barely any effect on the removals of ENT and AMT in the shake condition, indicating ethanol washing would not affect the adsorption of antibiotics. Meanwhile, ethanol treatment did not change the hydrodynamic diameter of materials in the US system (Fig. 5), suggesting that mass transfer was not influenced. The Fe crystalline phase was also not changed (Fig. S8). On the contrary, the removal efficiencies of ENT and AMT decreased by 11.4–38.9% and 19.7–29.1% for the SCM samples under the US condition, respectively. Cavitation played a crucial role in degrading antibiotics by SCM. The quantitative correlation between the structural characteristics and the reduced percentages of

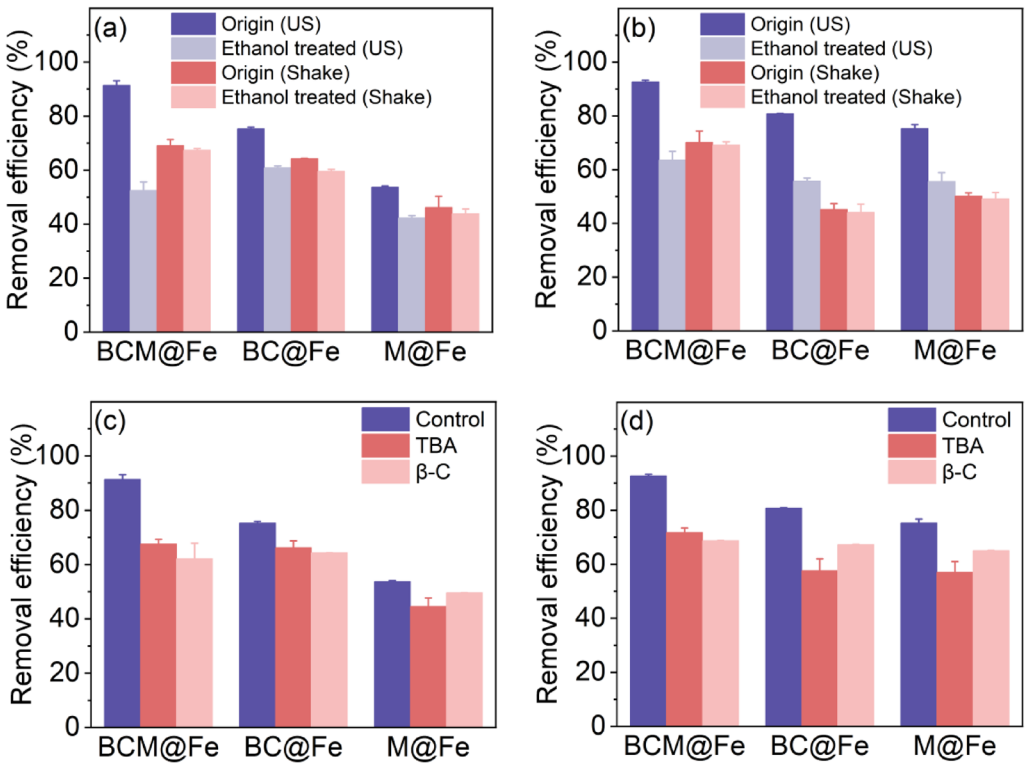

Fig. 8 Removals of ENT (**a**) and AMT (**b**) by BCM@Fe, BC@Fe, and M@Fe before and after ethanol treatment under shake and US systems; Effect of radical scavengers on ENT (**c**) and AMT (**d**) removal

ENT and AMT removals caused by cavitation was further analyzed (Fig. S9). Statistically, both the reduced removal percentages of ENT and AMT were significantly positively correlated with the bulk C content, pH, aromaticity, hydrophobicity and graphitization of the SCM ($R^2 = 1.000$, $p < 0.01$). Meanwhile, they also had a significantly negative correlation with the content of O containing groups ($R^2 = -1.000$, $p < 0.01$). Hence, SCM could tune and optimize the cavitation performance through structural modulation of covalently combined CNT and BC. Previous studies displayed that the mesoporous silica nanoparticles (Chen et al. 2017), TiO_2 (Jonnalagadda et al. 2022) and polymer nanocups (Kwan et al. 2018) could enhance the likelihood of cavitation because their porous structures endowed stable external nuclei for cavitation. However, no relationship with surface area was found in this study, suggesting that the role of porosity in the SCM on cavitation could be neglected.

It has been reported that ultrasound-derived ROS generated by inertial cavitation dominated the degradation of non-volatile organic compounds when the ultrasound frequency was 500 kHz (Joseph et al. 2000). Hence, EPR measurements were performed to detect the ROS during antibiotics removal. Hydroxyl radicals (•OH) and $^1O_2$ from SCM were not detected in the shake system (Fig. S10), but they were detected in US condition. Thus, SCM were activated by US and then enhanced the generation of •OH and $^1O_2$. On the one hand, Fe^0 reacted with O_2 to form H_2O_2 (Eq. 2). Further, Fe^0 and Fe^{2+} catalyzed H_2O_2 to produce •OH (Eqs. 3–4). On the other hand, the extremely high temperatures and pressures produced from collapsing cavitation bubbles in aqueous solution caused the water splitting to produce •OH (De Visscher et al. 1996) (Eq. 5). Then a small part of •OH migrated into the solution and some of them reacted with each other to generate H_2O_2 (Merouani et al. 2010). BCM@Fe possessed the highest hydrophobicity among the three materials (Fig. S7), and the hydrophobicity of ENT was higher than that of AMT, attributing to the larger Log*P* (Table S1), which resulted in the maximum distribution of ENT at the gas–liquid interface and then ENT was degraded by •OH (Goel et al. 2004). In contrast, AMT was inclined to dissolve and disperse in solution rather than remain at the gas–liquid interface (Karim and Shriwastav 2021). This meant that AMT tended to be degraded by •OH dissolved into solution which led to the lower TOC removal efficiencies than those of ENT.

$$Fe^0 + O_2 + 2H^+ \rightarrow Fe^{2+} + H_2O_2 \quad (2)$$

$$Fe^0 + 2H_2O_2 \rightarrow Fe^{2+} + 2 \cdot OH + 2OH^- \quad (3)$$

$$Fe^{2+} + H_2O_2 \rightarrow Fe^{3+} + \cdot OH + OH^- \quad (4)$$

$$H_2O \xrightarrow{))} \cdot OH + \cdot H \quad (5)$$

$$2 \cdot OH \rightarrow H_2O_2 \quad (6)$$

The generation of $^1O_2$ included free radical and non-free radical pathways (Wang et al. 2024a, b; Xie et al. 2023). In the non-free radical pathway, O_2 could be excited by sufficient energy which was supplied by US cavitation and transformed from ground state to excited state to form $^1O_2$. Besides, the graphitization degree of carbon-based materials was also important for the generation of $^1O_2$, because it enabled the prominent enhancement of electronic transfer between catalyst and O_2 (Ma et al. 2018; Wang et al. 2016; Yun et al. 2018). The graphitization degree of BCM@Fe was the highest as indicated by I_D/I_G values in Raman spectra (Fig. 2f), which led to the strongest signal intensities of $^1O_2$. Thus, the combination of CNT and BC as the support for Fe particles was beneficial to adsorb O_2 for the production of $^1O_2$. For the radical pathway, Fe^{3+} served as an effective catalyst to catalyze H_2O_2 for generating $^1O_2$ (Chong et al. 2017) (Eqs. 7–8).

$$Fe^{3+} + H_2O_2 \rightarrow Fe^{2+} + HO_2^{\cdot} + H^+ \quad (7)$$

$$2HO_2^{\cdot} \rightarrow {}^1O_2 + H_2O_2^- \quad (8)$$

To further elucidate ENT and AMT degradation mechanisms, the contributions of ROS were analyzed by quenching tests. Tert-butanol (TBA) and beta-carotene (β-C) were used as the scavengers for •OH and $^1O_2$, respectively. The results showed that the removal efficiencies of ENT by SCM reduced from 91.4–68.7% to 67.6–61.5% and 62.1–63.4% with the addition of 0.01 mM TBA and 0.05 mM β-C, respectively (Fig. 8c). Meanwhile, the AMT removal efficiencies declined by 22.5–28.7% and 13.7–25.9% for the three materials, respectively (Fig. 8d). Remarkably, the degradation efficiencies of ENT and AMT by BCM@Fe surpassed those of BC@Fe and M@Fe. BCM@Fe achieved a stronger cavitation effect under low frequency US irradiation, thus generating a higher concentration of ROS. The total contributions of •OH and $^1O_2$ to the degradation of ENT and AMT were 14.2% and 15.8% higher than those of cavitation by BCM@Fe, respectively, demonstrating that heat and mechanical effects from the collapsing bubble enhanced the catalytic activation of SCM and promoted ROS generation.

Thus, the removal pathways and mechanisms of ENT and AMT on BCM@Fe are shown in Fig. 9. ENT removal involved two pathways and these pathways operated concurrently: (1) Adsorption was a prerequisite step for ENT degradation. At first, ENT was adsorbed onto the material via π-π interaction, H bond, and hydrophobic interaction. Then, it was degraded by ROS generated on the material's surface due to cavitation and electron transfer. Adsorption occurred by enriching ENT molecules onto the material surface, shortening their mass transfer distance with cavitation bubbles/ROS, thereby accelerating degradation; (2) ENT in solution was directly degraded by •OH, $^1O_2$ and cavitation. The degradation processes primarily proceeded via ring-opening oxidation and reaction of degradation intermediates. AMT underwent similar degradation pathways to ENT, primarily involving ring-opening and subsequent oxidation of intermediate products. However, AMT was degraded in the liquid phase rather than on the material's surface. The desorption experiment indicated that few AMT molecules were adsorbed on the material, thus it was the degradation products that were adsorbed onto the material through π-π interaction, H bond, and hydrophobic interaction.

3.5 Possible degradation pathways of ENT and AMT

The antibiotic intermediates after the removals using BCM@Fe under US conditions were determined by UPLC-QTOF-MS/MS analysis (Figs. 10, 11, Figs. S11–20, Tables S6–7). The molecular weights of proposed structures closely match the detected values. Based on the reaction mechanism, characteristic fragment ions, and neutral losses, the possible degradation pathways were proposed. The typical chromatogram of ENT degradation is shown in Fig. S13. ENT in the positive ion mode with $m/z = 360.2$ was detected in the initial solution at retention time (RT) = 4.05 min and few intermediates were detected in liquid during the US degradation. Thus a mixture of methanol and aqueous ammonia (15% aqueous ammonia) was used to desorb the degradation intermediate products of ENT that had adsorbed on BCM@Fe at 6 h (Tang et al. 2019). According to the intermediate products in Table S6, the degradation pathways of ENT are proposed in Fig. 10.

In Pathway Ⅰ, the C–F bond of ENT was cracked and F was replaced by hydroxyl due to the presence of •OH. Thus, a typical fluoroquinolone oxidation intermediate of ENT 1 was produced by nucleophilic substitution. Then, an oxidative ring-opening reaction and decarboxylation occurred to produce ENT 2–4. In fact, the defluorination efficiency of ENT by BCM@Fe was only 5.22% at 6 h. BCM@Fe also exhibited high removal efficiencies for ciprofloxacin, ofloxacin and norfloxacin under US irradiation, but the defluorination efficiencies

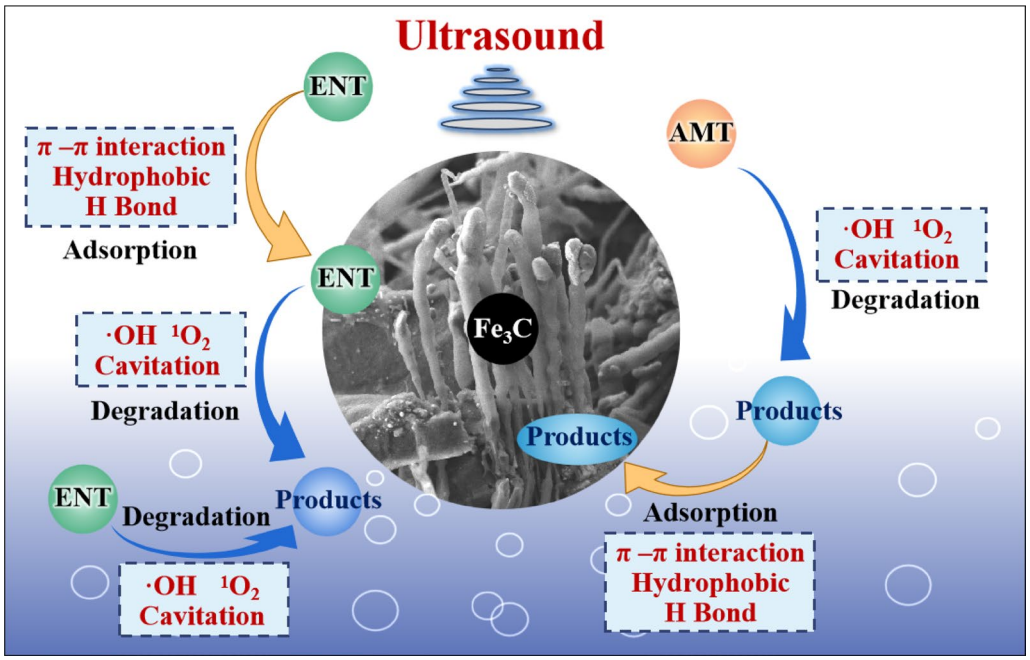

Fig. 9 Schematic representation of ENT and AMT removal mechanism by BCM@Fe

were only 7.99–9.90% (Fig. S21). The lower values suggested that defluorination might not be the major pathway because of the extremely high bond dissociation energy of the C–F bond (~ 485 kJ mol^{-1}) (Evich et al. 2022), which made the cleavage of fluorine atoms from the molecular backbone thermodynamically unfavorable under low-frequency US (40 kHz). Pathway II mainly involved the dehydrogenation oxidation of a piperazinyl group. The collapsing cavitation bubbles with extremely high temperatures led to the dehydrogenation reaction and ring-opening of the piperazine ring in ENT to form ENT 1' and ENT 2'. Pathway III described the oxidation destruction of the piperazinyl group to form ENT 5. Meanwhile, a potential nucleophilic substitution reaction was inferred, wherein the carboxylic group in the mother molecule might react with ammonia to form an amide. Subsequently, the loss of an ethyl group ($-C_2H_5$) from ENT 5, plausibly via a dealkylation process, yielded ENT 6. Further, hydroxyl replacement and deamination led to the formation of ENT 7. In Pathway IV-VI, the parent molecule might react with its degradation products — 1-ethyl-4-methylpiperazine, 4-fluoroaniline, and 1-N-cyclopropylbenzene-1,3-diamine— to form ENT 8, ENT 8', and ENT 12, respectively (Fig. S11). Then, dehydrogenation oxidation and demethylation reaction were further induced to produce ENT 9–11. Both Pathways IV and VI involved the nucleophilic replacement of F by an amino group.

The liquid chromatogram in Fig. S18 displayed that the positive mode of AMT with m/z = 366 was detected at RT = 2.62 min and some degradation products were produced at 10 min. Table S7 listed the possible intermediate products of AMT and the degradation pathways are shown in Fig. 11. In Pathway I, the hydrolysis of AMT primarily involved a nucleophilic attack on the carbonyl carbon of the four-membered ß-lactam ring, leading to ring opening and formation of AMT 1, concomitant with oxidation of the ketone moiety to a carboxylic acid. Subsequently, decarboxylation (the loss of –COOH) and further ring opening reactions occurred, leading to the transformation of AMT 1 into AMT 5 or AMT 5'. AMT 1 degraded to AMT 2 through a series of chemical reactions including dehydrogenation oxidation and deamination. After successive decarboxylation and dehydrogenation reactions, AMT 3 and AMT 4 were obtained, respectively. Finally, AMT 6 was produced by C–N bond breaking. In Pathway II, deamidation and dehydrogenation oxidation caused the production of AMT 7. Then, AMT 7 could be further degraded to form AMT 2, 3, 4, and 6. Meanwhile, the amide bond hydrolysis and further oxidation could also result in the direct formation of AMT 8 (Pathway III). The US degradation also resulted in the formation of the oxidation product of AMT 9 (Pathway IV).

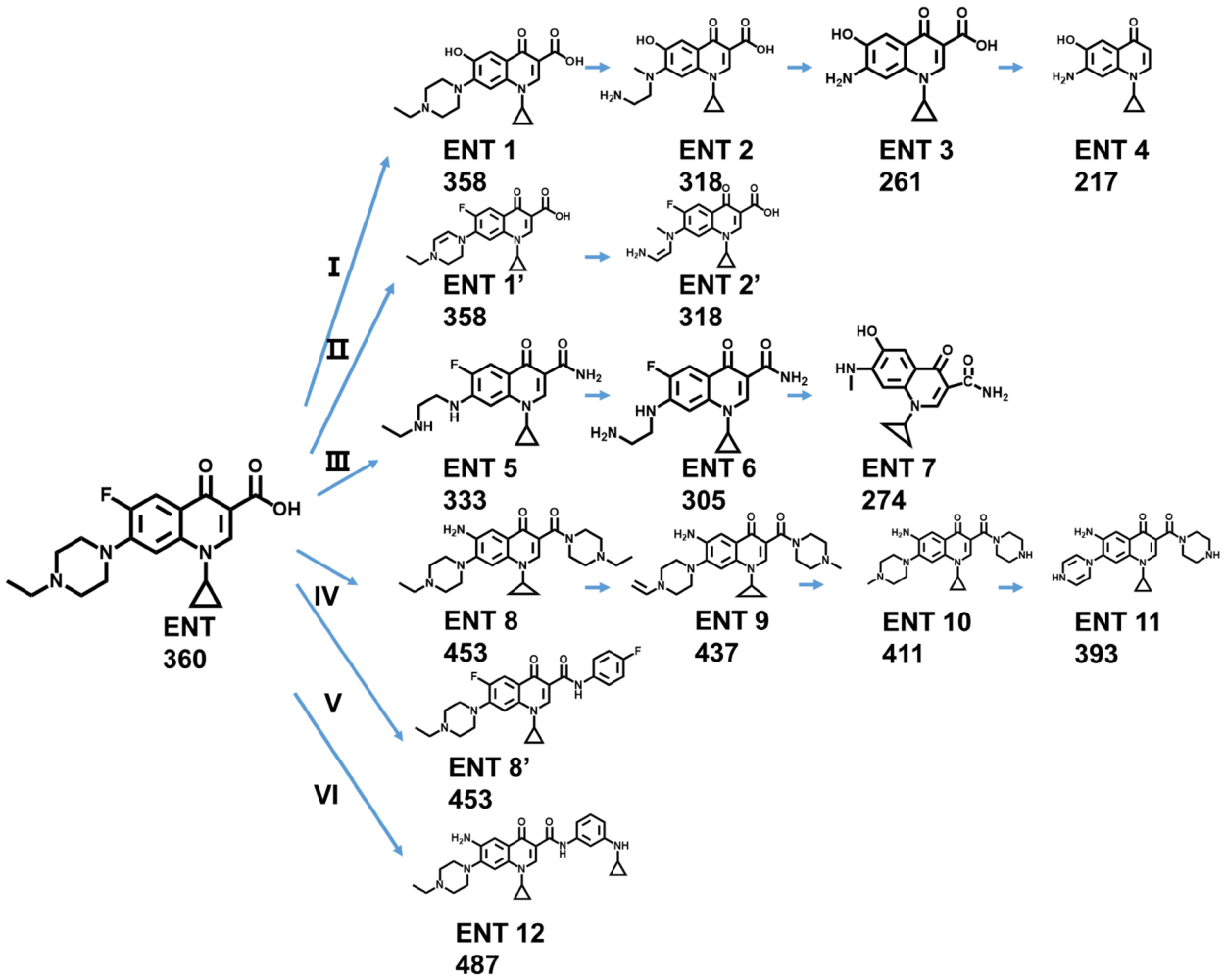

Fig. 10 Proposed degradation pathways of ENT by BCM@Fe

3.6 Practical application and reuse performance evaluation

The treatment of ENT and AMT in tap water was conducted to assess the practical application of BCM@Fe in the US system and the water quality information is shown in Table S9. As shown in Fig. S22, the removal efficiencies of antibiotics were slightly reduced and they were 80% and 72.7% for ENT and AMT, respectively. This might be because Ca^{2+}, Na^{+}, Mg^{2+} and K^{+} in tap water could be adsorbed by BCM@Fe, competing for the adsorption sites (Sun et al. 2019). But US could clean the surface, allowing the system to maintain high removal efficiencies. The TOC removal efficiency for ENT and AMT decreased by 15.3% and 11.3%, respectively. The decline might be because the dissolved organic matters (DOM) present in tap water competed with pollutants for •OH (Yu et al. 2022). Within the 1 h, the removal efficiency of ENT decreased slightly by 0.89%, while that of AMT declined more significantly by 9.60%, suggesting that AMT is more susceptible to cation interference at the initial reaction stage (Fig. S22c–d). After 6 h of reaction, the removal efficiencies of ENT and AMT decreased by 6.0% and 14.8%, respectively. Notably, the BCM@Fe/US system demonstrates robust practical applicability for antibiotic removal in real tap water.

The reusability of BCM@Fe was evaluated over five cycles in US systems (Fig. 12). As shown in Fig. 12a, the removal efficiency of ENT on BCM@Fe increased compared with the first reaction. Meanwhile, the removal efficiencies of AMT remained higher than 90% after 5 cycles. This was because high temperature desorption realized the reactivation of the C/Fe composite, thereby improving its performance. The XRD results showed that the Fe_3C phase was still observed after 6 cycles of reactions in US systems and the leaching Fe concentration of BCM@Fe (0.10–0.29 mg L^{-1}) was far below the USEPA's secondary drinking water standard (0.3 mg L^{-1}).

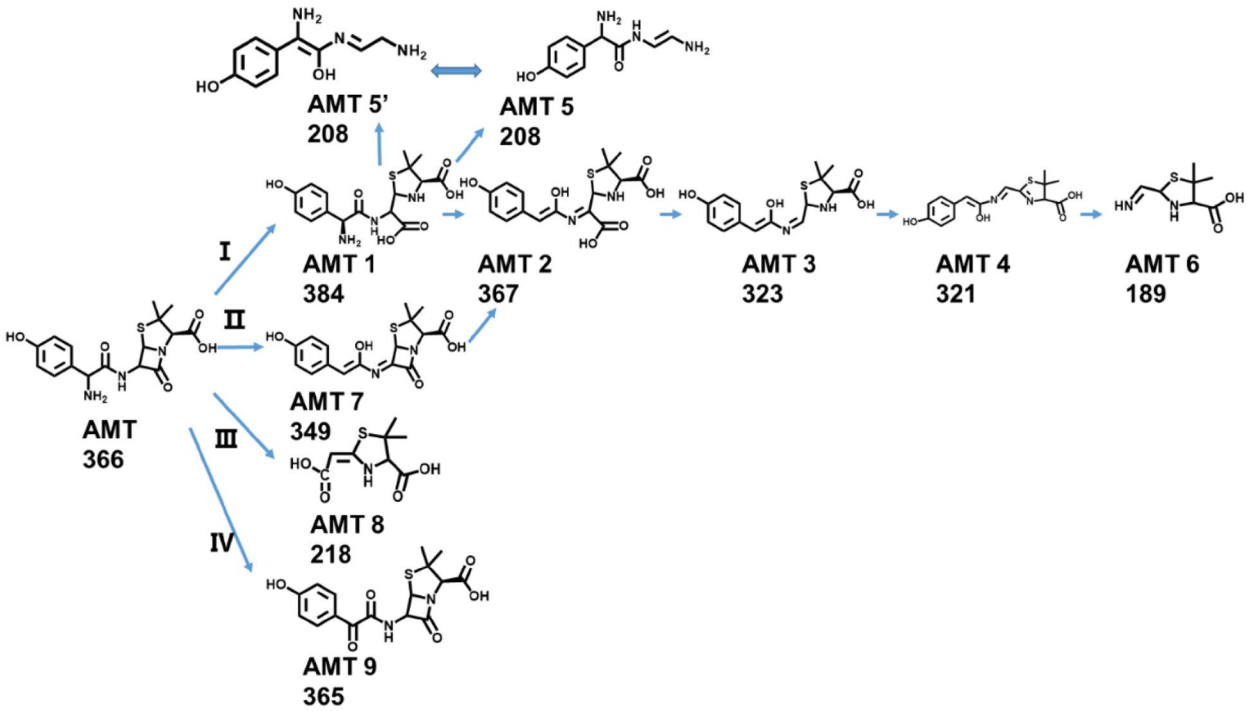

Fig. 11 Proposed degradation pathways of AMT by BCM@Fe

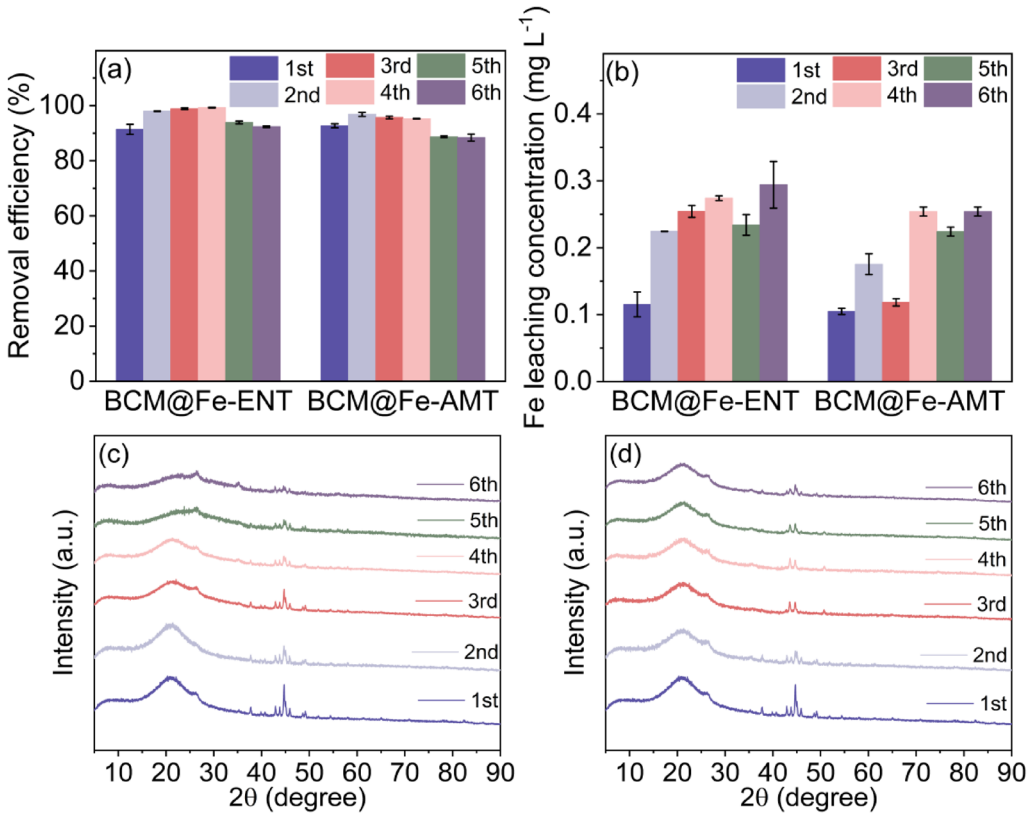

Fig. 12 Removal of ENT and AMT by BCM@Fe in five successive cycles (**a**), Fe leaching concentration (**b**) and the XRD patterns of BCM@Fe with the reaction of ENT (**c**) and AMT (**d**) before each cycles

These results demonstrated that BCM@Fe is a promising catalyst for the removal of antibiotics in US systems.

4 Conclusions

In an effort to enhance the removal ability of recalcitrant antibiotics by the M@Fe composite, a new solid cavitation material, BCM@Fe composite, was first developed for the removal of ENT and AMT under low frequency ultrasound. Based on the experimental results and DFT calculation, the underlying mechanisms for the formation of BCM@Fe composite were deeply elucidated and CNT was covalently bonded with BC. The introduction of BC gave the BCM@Fe composite significant advantages for ENT and AMT removal over M@Fe and BC@Fe in both US and shake systems. Moreover, it exhibited the best ENT and AMT removal capacities under pH-universal conditions (acidic, neutral, and alkaline), and demonstrated excellent recycling performance. There were hydrophobic, π-π interactions and H bonds between ENT/AMT and BCM@Fe for the adsorption process. The presence of BC in BCM@Fe significantly enhanced US-triggered cavitation, and the activation of BCM@Fe by heat and mechanical effects led to amplified generation of ROS for the degradation of ENT and AMT. Such a study would advance the understanding about the formation mechanism of Fe based combined carbonaceous materials and more concretely link the cavitation effect to ROS generation and the intrinsic nature of the materials.

Supplementary Information

The online version contains supplementary material available at https://doi.org/10.1007/s42773-025-00551-2.

Supplementary material 1.

Author contributions

Ao Wang: Methodology, Investigation, Data curation, Writing–original draft. Nan Zhao: Methodology, Investigation, Data curation, Writing–original draft, Funding acquisition. Lei He: Investigation, Data curation. Ye Xiao: Writing–review & editing, Funding acquisition. Chuanfang Zhao: Methodology, Data curation. Siyuan Guo: Investigation. Xiang Liu: Writing–review & editing. Weihua Zhang: Writing–review & editing. Kunyuan Liu: Methodology, Data curation, Writing–review & editing. Rongliang Qiu: Writing–review & editing.

Funding

This project was supported by National Key Research and Development Program of China (2019YFC1803900), GDAS' Project of Science and Technology Development (2023GDASZH-2023010103), Natural Science Foundation of Guangdong Province (2023A1515012279), Science and Technology Program of Guangzhou (202201011177), Guangdong Foundation for Program of Science and Technology Research (2023B1212060044).

Data availability

Data will be made available on request.

Declarations

Competing interests

The authors declare that they have no known competing financial interests or personal relationships that could have appeared to influence the work reported in this paper.

Author details

[1]School of Environmental Science and Engineering, Guangdong Provincial Key Lab of Environmental Pollution Control and Remediation Technology, Sun Yat-Sen University, Guangzhou 510275, People's Republic of China. [2]Guangdong Key Laboratory of Integrated Agro-Environmental Pollution Control and Management, Institute of Eco-Environmental and Soil Sciences, National-Regional Joint Engineering Research Center for Soil Pollution Control and Remediation in South China, Guangdong Academy of Sciences, Guangzhou 510650, China. [3]Guangzhou Institute of Energy Conversion, Chinese Academy of Sciences, Guangzhou 510640, People's Republic of China. [4]Research Center for Eco-Environmental Sciences, Chinese Academy of Sciences, Beijing 100085, China. [5]College of Materials and Chemical Engineering, Ministry of Education, Key Laboratory of Inorganic Nonmetallic Crystalline and Energy Conversion Materials, Engineering Research Center of Eco-Environment in Three Gorges Reservoir Region, China Three Gorges University, Yichang, Hubei 443002, People's Republic of China. [6]Guangdong Laboratory for Lingnan Modern Agriculture, Guangdong Provincial Key Laboratory of Agricultural & Rural Pollution Abatement and Environmental Safety, College of Natural Resources and Environment, South China Agricultural University, Guangzhou 510642, People's Republic of China.

Received: 7 April 2025 Revised: 28 October 2025 Accepted: 10 November 2025
Published online: 09 February 2026

References

Bergamonti L, Bergonzi C, Graiff C, Lottici PP, Bettini R, Elviri L (2019) 3D printed chitosan scaffolds: a new TiO_2 support for the photocatalytic degradation of amoxicillin in water. Water Res 163:114841

Çakmakçı N, Yoo B, Lee H, Jeong Y (2024) Assessment of carbon nanotube sheet densification level. Carbon Lett 34:1239–1245

Chen Z, Wannere CS, Corminboeuf C, Puchta R, Schleyer PVR (2005) Nucleus-Independent Chemical Shifts (NICS) as an Aromaticity Criterion. Chem Rev 105:3842–3888

Chen F, Ma M, Wang J, Wang F, Chern S, Zhao ER, Jhunjhunwala A, Darmadi S, Chen H, Jokerst JV (2017) Exosome-like silica nanoparticles: a novel ultrasound contrast agent for stem cell imaging. Nanoscale 9:402–411

Chong S, Zhang G, Zhang N, Liu Y, Huang T, Chang H (2017) Diclofenac degradation in water by FeCeOx catalyzed H_2O_2: influencing factors, mechanism and pathways. J Hazard Mater 334:150–159

Cui H, Zhan W, Ji X, Jiang M, Wu X, Huang M, Huang C, Ma S (2023) Removal of sulfonamide antibiotics by a sonocatalytic fenton-like reaction: efficiency and mechanisms. Environ Res 239:117408

De Visscher A, Van Eenoo P, Drijvers D, Van Langenhove H (1996) Kinetic model for the sonochemical degradation of monocyclic aromatic compounds in aqueous solution. J Phys Chem 100:11636–11642

Dehghan S, Kakavandi B, Kalantary RR (2018) Heterogeneous sonocatalytic degradation of amoxicillin using ZnO@Fe_3O_4 magnetic nanocomposite: influential factors, reusability and mechanisms. J Mol Liq 264:98–109

Dou M, Wang J, Gao B, Xu C, Yang F (2020) Photocatalytic difference of amoxicillin and cefotaxime under visible light by mesoporous g-C3N4: mechanism, degradation pathway and DFT calculation. Chem Eng J 383:123134

Evich MG, Davis MJB, Mccord JP, Acrey B, Awkerman JA, Knappe DRU, Lindstrom BL, Speth TF, Tebes C, Stpynar MJ, Wang Z, Weber EJ, Henderson WM, Washington JW (2022) Per- and polyfluoroalkyl substances in the environment. Science 375:6580

Farshbaf Aghajani P, Soltani Firouz M, Alikhani Chamgordani P (2023) The improvement of freezing time and functional quality of frozen mushrooms by application of probe-type power ultrasound. Ultrason Sonochem 100:106637

Flint EB, Suslick KS (1991) The temperature of cavitation. Science 253:1397–1399
Fontana RJ, Shakil AO, Gerrnson JK, Boyd I, Lee WM (2005) Acute liver failure due to amoxicillin and amoxicillin/clavulanate. Dig Dis Sci 50:1785–1790
Francisco PCM, Mitsui S, Ishidera T, Tachi Y, Doi R, Shiwaku H (2020) Interaction of FeII and Si under anoxic and reducing conditions: structural characteristics of ferrous silicate co-precipitates. Geochim Cosmochim Acta 270:1–20
Geng C, Chen Q, Li Z, Liu M, Chen Z, Tao H, Yang Q, Zhu B, Feng L (2023) Degradation of enrofloxacin by a novel Fe–N–C@ZnO material in freshwater and seawater: performance and mechanism. Environ Res 237:116960
Gholami M, Rahmani K, Rahmani A, Rahmani H, Esrafili A (2016) Oxidative degradation of clindamycin in aqueous solution using nanoscale zero-valent iron/H_2O_2/US. Desalin Water Treat 57:13878–13886
Goel M, Hongqiang H, Mujumdar AS, Ray MB (2004) Sonochemical decomposition of volatile and non-volatile organic compounds—a comparative study. Water Res 38:4247–4261
Grilla E, Vakros J, Konstantinou I, Manariotis ID, Mantzavinos D (2020) Activation of persulfate by biochar from spent malt rootlets for the degradation of trimethoprim in the presence of inorganic ions. J Chem Technol Biotechnol 95:2348–2358
Gutiérrez M, Henglein A, Fischer CH (1986) Hot spot kinetics of the sonolysis of aqueous acetate solutions. Int J Radiat Biol Relat Stud Phys Chem Med 50:313
Hontoria-Lucas C, López-Peinado AJ, López-González JDD, Rojas-Cervantes ML, Martín-Aranda RM (1995) Study of oxygen-containing groups in a series of graphite oxides: physical and chemical characterization. Carbon 33:1585–1592
Inyang M, Gao B, Zimmerman A, Zhou Y, Cao X (2015) Sorption and cosorption of lead and sulfapyridine on carbon nanotube-modified biochars. Environ Sci Pollut Res 22:1868–1876
Jonnalagadda US, Fan Q, Su X, Liu W, Kwan JJ (2022) Nanostructured sonophotocatalysts for spatially controlled inertial cavitation towards energy-efficient sonochemistry. ChemCatChem 14:e202200732
Joseph JM, Destaillats H, Hung H, Hoffmann MR (2000) The sonochemical degradation of azobenzene and related azo dyes: rate enhancements via Fenton's reactions. J Phys Chem A 104:301–307
Karim AV, Shriwastav A (2021) Degradation of amoxicillin with sono, photo, and sonophotocatalytic oxidation under low-frequency ultrasound and visible light. Environ Res 200:111515
Kowalska J, Banach K, Beberok A, Rok J, Rzepka Z, Wrześniok D (2021) The biochemical and molecular analysis of changes in melanogenesis induced by UVA-activated fluoroquinolones—in vitro study on human normal melanocytes. Cells 10:2900
Kwan JJ, Lajoinie G, Stride EP, Versluis M, Coussios C (2018) The induction of inertial cavitation from polymeric nanocups—from theory to observation. J Acoust Soc Am 143:1834
Li H, Zhang D, Han X, Xing B (2014) Adsorption of antibiotic ciprofloxacin on carbon nanotubes: pH dependence and thermodynamics. Chemosphere 95:150–155
Li Z, Li M, Zhang Z, Li P, Zang Y, Liu X (2020) Antibiotics in aquatic environments of China: a review and meta-analysis. Ecotox Environ Safe 199:110668
Li S, Jin W, Jiang H, Zhang H, Kong D, Zhu L (2024) Efficient removal of phenanthrene by covalent organic frameworks: an experimental combined with theoretical analysis. Sep Purif Technol 336:126189
Liu K, Zhao D, Hu Z, Xiao Y, He C, Jiang F, Zhao N, Zhao C, Zhang W, Qiu R (2023a) The adsorption and reduction of anionic Cr(VI) in groundwater by novel iron carbide loaded on N-doped carbon nanotubes: effects of Fe-confinement. Chem Eng J 452:139357
Liu P, Wu Z, Fang Z, Cravotto G (2023b) Sonolytic degradation kinetics and mechanisms of antibiotics in water and cow milk. Ultrason Sonochem 99:106518
Lu Y, Zhou X, Zheng Y, Yang H, Cao W (2025) How far do we still need to go with antibiotics in aquatic environments? Antibiotic occurrence, chemical-free or chemical-limited strategies, key challenges, and future perspectives. Water Res 275:123179
Luan J, Liu W, Yao Y, Ma B, Niu B, Yang G, Wei Z (2022) Synthesis and property examination of Er_2FeSbO_7/$BiTiSbO_6$ heterojunction composite catalyst and light-catalyzed retrogradation of enrofloxacin in pharmaceutical waste water under visible light irradiation. Materials 15:5906
Ma W, Wang N, Fan Y, Tong T, Han X, Du Y (2018) Non-radical-dominated catalytic degradation of bisphenol A by ZIF-67 derived nitrogen-doped carbon nanotubes frameworks in the presence of peroxymonosulfate. Chem Eng J 336:721–731
Maguire CM, Rösslein M, Wick P, Prina-Mello A (2018) Characterisation of particles in solution-a perspective on light scattering and comparative technologies. Sci Technol Adv Mat 19:732–745
Meroni D, Djellabi R, Ashokkumar M, Bianchi CL, Boffito DC (2022) Sonoprocessing: from concepts to large-scale reactors. Chem Rev 122:3219–3258
Merouani S, Hamdaoui O, Saoudi F, Chiha M (2010) Sonochemical degradation of Rhodamine B in aqueous phase: effects of additives. Chem Eng J 158:550–557
Peng Z, Xiong C, Wang W, Tan F, Wang X, Qiao X, Wong PK (2018) Hydrophobic modification of nanoscale zero-valent iron with excellent stability and floatability for efficient removal of floating oil on water. Chemosphere 201:110–118
Peng G, Li T, Ai B, Yang S, Fu J, He Q, Yu G, Deng S (2019) Highly efficient removal of enrofloxacin by magnetic montmorillonite via adsorption and persulfate oxidation. Chem Eng J 360:1119–1127
Rahmani H, Gholami M, Mahvi AH, Alimohammadi M, Azarian G, Esrafili A, Rahmani K, Farzadkia M (2014) Tinidazole removal from aqueous solution by sonolysis in the presence of hydrogen peroxide. B Environ Contam Toxicol 92:341–346
Rangraz Y, Heravi MM (2021) Recent advances in metal-free heteroatom-doped carbon heterogonous catalysts. RSC Adv 11:23725–23778
Sapalidis A, Sideratou Z, Panagiotaki KN, Sakellis E, Kouvelos EP, Papageorgiou S, Katsaros F (2018) Fabrication of antibacterial poly(vinyl alcohol) nanocomposite films containing dendritic polymer functionalized multi-walled carbon nanotubes. Front Mater. https://doi.org/10.3389/fmats.2018.00011
Serna-Galvis EA, Celis-Llamoca KP, Collantes-Díaz IE, Torres-Palma RA, Nieto-Juárez JI (2025) Insights into the transformations, antimicrobial activity, and degradation efficiency of a representative carbapenem antibiotic by high-frequency ultrasound hybridized with the (photo) Fenton process. Ultrason Sonochem 119:107379
Shan L, Gao M, Pan X, Li W, Wang J, Li H, Tian H (2022) Association between fluoroquinolone exposure and children's growth and development: a multisite biomonitoring-based study in northern China. Environ Res 214:113924
Singh R, Kim K (2025) Environmental occurrence of antibiotic resistance, control measures and challenges in finding therapeutic management. Emerg Contam 11:100440
Stride E, Coussios C (2019) Nucleation, mapping and control of cavitation for drug delivery. Nat Rev Phys 1:495–509
Sun Y, Yu IKM, Tsang DCW, Cao X, Lin D, Wang L, Graham NJD, Alessi DS, Komárek M, Ok YS, Feng Y, Li X (2019) Multifunctional iron-biochar composites for the removal of potentially toxic elements, inherent cations, and hetero-chloride from hydraulic fracturing wastewater. Environ Int 124:521–532
Tan C, Liu Y, He Y, Luo W, Zhang R, Vijver MG, Peijnenburg WJGM (2021) The relative contributions of complexation, dispersing, and adsorption of tannic acid to the dissolution of copper oxide nanoparticles. Water Air Soil Pollut 232:359
Tang H, Wang Y, Li S, Wu J, Li J, Zhou H, Gao Z (2019) Graphene oxide composites for magnetic solid-phase extraction of twelve quinolones in water samples followed by MALDI-TOF MS. Anal Bioanal Chem 411:7039–7049
Thomas RG, Jonnalagadda US, Kwan JJ (2019) Biomedical applications for gas-stabilizing solid cavitation agents. Langmuir 35:10106–10115
Wada OZ, Olawade DB (2025) Recent occurrence of pharmaceuticals in freshwater, emerging treatment technologies, and future considerations: a review. Chemosphere 374:144153
Wang H, Jiang S, Chen S, Li D, Zhang X, Shao W, Sun X, Xie J, Zhao Z, Zhang Q, Tian Y, Xie Y (2016) Enhanced singlet oxygen generation in oxidized graphitic carbon nitride for organic synthesis. Adv Mater 28:6940–6945
Wang J, Hui X, Liu H, Dai X (2024a) Classification, characteristics, harmless treatment and safety assessment of antibiotic pharmaceutical wastewater (APWW): a comprehensive review. Chemosphere 366:143504
Wang Y, Lin Y, He S, Wu S, Yang C (2024b) Singlet oxygen: properties, generation, detection, and environmental applications. J Hazard Mater 461:132538

Wu B, Meng H, Morales DM, Zeng F, Zhu J, Wang B, Risch M, Xu ZJ, Petit T (2022) Nitrogen-rich carbonaceous materials for advanced oxygen electrocatalysis: synthesis, characterization, and activity of nitrogen sites. Adv Funct Mater 32:2204137

Xie Z, He C, Pei D, Dong Y, Yang S, Xiong Z, Zhou P, Pan Z, Yao G, Lai B (2023) Review of characteristics, generation pathways and detection methods of singlet oxygen generated in advanced oxidation processes (AOPs). Chem Eng J 468:143778

Yang Z, Qian J, Yu A, Pan B (2019) Singlet oxygen mediated iron-based Fenton-like catalysis under nanoconfinement. Proc Natl Acad Sci 116:6659–6664

Yi C, Shang J, Shen Z, Sun Y, Yang Y, Zheng X, Peng Z, Chen J, Liu Y, Guo R, Liao Q (2025) Distribution and risk characteristics of antibiotics in China surface water from 2013 to 2024. Chemosphere 375:144197

Yu Z, Ma J, Huang X, Lv Y, Liu Y, Lin C, Dou R, Ye X, Shi Y, Liu M (2022) Insights into enhanced peroxydisulfate activation with S doped Fe@C catalyst for the rapid degradation of organic pollutants. J Colloid Interf Sci 610:24–34

Yun E, Lee JH, Kim J, Park H, Lee J (2018) Identifying the nonradical mechanism in the peroxymonosulfate activation process: singlet oxygenation versus mediated electron transfer. Environ Sci Technol 52:7032–7042

Zhang W, Fu Y, Liu W, Lim L, Wang X, Yu A (2019) A general approach for fabricating 3D MFe_2O_4 (M=Mn, Ni, Cu, Co)/graphitic carbon nitride covalently functionalized nitrogen-doped graphene nanocomposites as advanced anodes for lithium-ion batteries. Nano Energy 57:48–56

Zhang S, Zhang S, Rong F, Huang S, Zhao S, Wang M, He L, Zhang Z, Du M (2022) Atomic Fe sites embedded within carbon nanotubes for the efficient photodegradation of multiple tetracyclines. Sep Purif Technol 287:120530

Zhao N, Chang F, Hao B, Yu L, Morel JL, Zhang J (2019) Removal of organic dye by biomass-based iron carbide composite with an improved stability and efficiency. J Hazard Mater 369:621–631

Zhao N, Liu K, He C, Gao J, Zhang W, Zhao T, Tsang DCW, Qiu R (2020) Singlet oxygen mediated the selective removal of oxytetracycline in $C/Fe_3C/Fe^0$ system as compared to chloramphenicol. Environ Int 143:105899

Zhao N, Zhao C, Liu K, Zhang W, Tsang DCW, Yang Z, Yang X, Yan B, Morel JL, Qiu R (2021) Experimental and DFT investigation on N-functionalized biochars for enhanced removal of Cr(VI). Environ Pollut 291:118244

Zhao N, Tan X, Xiong J, Chen N, Gao J, Wang R, Yang X, Zhang W, Qiu R (2022) Quantitative analysis on the redox conversion mechanism of Cr(VI) and As(III) by iron carbide based biochar composites. Chem Eng J 446:137417

Zhao C, Meng L, Chu H, Wang J, Wang T, Ma Y, Wang C (2023) Ultrafast degradation of emerging organic pollutants via activation of peroxymonosulfate over Fe_3C/Fe@N-C-x: singlet oxygen evolution and electron-transfer mechanisms. Appl Catal B-Environ 321:122034

Zhao J, Yang X, Yang Y, Liu L, Lin Y, Xie L, Chai X, Xu K, Du G, Zhang L (2024a) Biomass polyamine-functionalized nanocellulose-loaded covalent organic framework to construct composite aerogels for highly efficient removal of Cr (VI) and methyl orange. Chem Eng J 486:150282

Zhao N, Wang A, Xiao Y, Zhao D, Zhao C, Yin Z, Zhang W, Zhang W, Qiu R, Xing B (2024b) Fe crystalline phases in Fe/C composites modulated the selective adsorption of Pb(II) from industrial wastewater with Cd(II): an electronic-scale perspective. Inorg Chem 63:15679–15691